Nanoscale Advances

ROYAL SOCIETY OF CHEMISTRY

PAPER

View Article Online
View Journal | View Issue

Cite this: *Nanoscale Adv.*, 2023, **5**, 3761

Highly selective CO_2 sensing response of lanthanum oxide nanoparticle electrodes at ambient temperature

Amutha Eswaran,[a] Madhumitha Thirumalainambi,[a] Rajaduraipandian Subramaniam[b] and Gurusamy Annadurai *[a]

Received 27th March 2023
Accepted 19th May 2023

DOI: 10.1039/d3na00199g

rsc.li/nanoscale-advances

Lanthanum oxide nanoparticles (La_2O_3 NPs) are attractive rare earth metal oxides because of their applications in optical devices, catalysts, dielectric layers, and sensors. Herein, we report room temperature operative carbon dioxide gas sensing electrodes developed by a simple sonication assisted hydrothermal method. The physiochemical, morphological and gas-sensing properties of the prepared nanoparticles were studied systematically and their successful preparation was confirmed with the absence of impurities and high selectivity towards CO_2. The fabricated sensor showed a high sensitivity of 40% towards CO_2 at 50 ppm, and it can detect concentrations of up to 5 ppm with a quick response time of 6 s and recovery of 5 s. The electrode demonstrated long-term stability of 95% for 50 days when tested with an interval of 10 days. This simple and cost-effective method shows great potential for fabricating room temperature CO_2 gas sensors.

Introduction

Carbon dioxide (CO_2) is a colourless and odourless greenhouse gas that is essential for living beings. The amount of CO_2 in the atmosphere is gradually increasing and has become a major crisis.[1] Nanostructured materials offer improved degradation efficiencies in comparison with both micro and bulk materials because they provide good characteristic outcomes through a quantum containment effect.[2] Lanthanum oxide nanoparticles (LaO NPs), a rare earth metal oxide, have unique properties that make them a suitable candidate for several electrical and biomedical applications.[3,4] Probes coated with LaO NPs are being developed as implantable sensors for various molecules such as glucose, phosphate and uric acid.[5] They are also used as a p-type semiconductor and have several other applications in the areas of electronics, fuel cells, optics, magnetic data storage, ceramics, catalysis, automobiles, biosensors, water treatment and biomedicine.[6,7] Lanthanum oxide (La_2O_3) is widely used because of its admirable chemical and physical properties[8] and it has been synthesized *via* the solution combustion method. It has a band gap of 5.8 eV and a high dielectric constant ($\varepsilon = 27$).[9]

The performance of a semiconductor material, when employed as a gas sensor, depends mainly on its operating temperature, the gas concentration, and the size and morphology of the component particles.[10] When the particles are nanometer-sized, the material's sensitivity increases substantially. Generally, sensors are devices that convert physical and chemical data into electrical signals.[11] A sensor is a component of an electronic circuit that senses and transfers the physical and chemical changes on its surface due to the adsorption of the chemical species. These adsorbed chemical species change the electrical conductivity of the sensor and then convert these changes into measurable signals.[12]

The currently available CO_2 sensors based on infrared spectroscopic analyzers and electrochemical and thermal conductivity detecting principles are commonly used. However, they have some limitations and disadvantages such as their large size, high cost, complex fabrication process, slow response, and unreliability, there is a need to develop inexpensive and maintenance-free CO_2 sensors.[13] Solid-state gas sensors based on semiconductor metal oxides provide a promising alternative since they offer good sensor properties and can be easily mass-produced.[14]

Recently, CO_2 gas sensors have been developed by many researchers. For example, S. Naama *et al.* reported a study on the synthesis of silicon nanowires modified with metal nanoparticles as a CO_2 sensor.[15] Irmak Karaduman and co-workers synthesized a UV light-irradiated TiO_2/Al_2O_3 heterostructure for CO_2 gas detection.[16] Muhammed Habib *et al.* prepared ZnO nanowires by a sol–gel method and used them for CO_2 gas sensing.[17] C. Willa studied a rare earth metal-free composite for a room temperature CO_2 sensor, which was lightweight and flexible.[18] M. A. Basyooni prepared various mixed valence

[a]*Sri Paramakalyani Centre of Excellence in Environmental Sciences, Manonmaniam Sundaranar University, Alwarkurichi – 627412, India. E-mail: gannadurai@msuniv.ac.in*

[b]*Sri Paramakalyani College, Manonmaniam Sundaranar University, Alwarkurichi – 627412, India*

phases in molybdenum and tungsten oxide nanostructured films using sputtering techniques and studied the fast response CO_2 sensor.[19]

La_2O_3 is effective in improving the activity and stability of the catalysts.[8] Alkali metal-based nanoparticles have been used as promoters for enhancing the activity, selectivity or stability in many catalytic reactions.[20] Photocatalytic reactions catalyzed by semiconductors have been approved as a promising process for solving energy and environmental issues. Among the semiconductor catalysts, La_2O_3 has been studied extensively due to its special properties. The antibacterial activities of La_2O_3 nanoparticles were tested against Gram-positive and Gram-negative bacteria using the well diffusion method.[21] The nanoparticles produced herein can be potentially used in the development of drug labels and other antibacterial agents.[22]

The primary challenge investigated in this study was to determine the ratio of La_2O_3 nanoparticles for making a reliable gas-sensing electrode that is highly sensitive towards CO_2. The oxide nanostructure was formed as a p–n junction layer for electron sensitization when the gas molecules interact with it. The La_2O_3 nanoparticles were used to investigate the structural properties, antibacterial efficiency against pathogenic bacteria, and catalytic activity toward the photodegradation of rhodamine dye of the resulting products in an attempt to provide an approach that can yield affordable products for water treatment purposes.

Materials and methods

Chemicals, reagents, and media

The analytical grade lanthanum nitrate, sodium lauryl sulphate, and ammonia solution were obtained from Sigma Aldrich Pvt Ltd, in India. Gram-positive *Staphylococcus aureus* and *Bacillus subtilis*, as well as Gram-negative *Escherichia coli*, *Enterobacter*, and *Pseudomonas fluorescens*, were obtained from the MTCC in Chandigarh as bacterial isolates.

Synthesis of La_2O_3 nanoparticles

The following method has been used to create La_2O_3 nanoparticles. During magnetic stirring, lanthanum nitrate hexahydrate was dissolved in 12.5 ml of distilled water to produce a 0.06 M solution. Dropwise additions of ammonia were made to keep the pH of the solution between 9 and 10, and this solution was added to 12.5 ml of sodium lauryl sulphate aqueous solution. The mixture was put into a 100 ml Teflon autoclave, sealed, and kept at 120 °C for 3 hours before being allowed to cool naturally to ambient temperature. The resulting precipitate was centrifuged separately, repeatedly rinsed with distilled water and ethanol, and then calcined for one hour at 600 °C (Fig. 1).

Fabrication of the sensing electrode

PCB was used as the active substrate in the fabrication of the gas-sensing electrode. After cleaning the PCB conducting layer, a 1 cm^2 section was prepared for the contact channel by being drawn with a positive resist. The piece was then dipped into the $FeCl_3$ solution to begin the etching process. The resist substance was removed using acetone. Lastly, a spin coater operating at 4000 revolutions per minute for 5 minutes covered the substrate with the sensing material. Electrodes were dried in a vacuum oven at 80 °C for 30 minutes. Single-core wires were connected at the terminals that would be attached to the voltage source for the sensor measurements.

Antibacterial properties

Agar well diffusion assay. The antibacterial properties of the lanthanum oxide NPs were examined By employing bacterial species including harmful bacteria like Gram-positive *Staphylococcus aureus* and *Bacillus subtilis*, as well as the Gram-negative *Escherichia coli*, *Enterobacter*, and *Pseudomonas fluorescens*. To determine the antibacterial activity of the above-mentioned bacterial species, different concentrations in 25, 50, 75, and 100 μl were tested. The zones of inhibition of the bacteria on each plate were assessed after 24 hours of incubation at 37 °C.

Photocatalytic activity. To examine the photocatalytic activity, 0.1 g of La_2O_3 NPs (catalyst) was added to 100 mL of Rhodamine solution (30 mg L^{-1}). A high-pressure UV lamp was used as the light source. The Rhodamine aqueous solution along with loaded La_2O_3 NPs was stirred for 80 min to confirm the adsorption–desorption equilibrium of Rhodamine dye molecules on the surface of the catalyst. To remove the catalyst

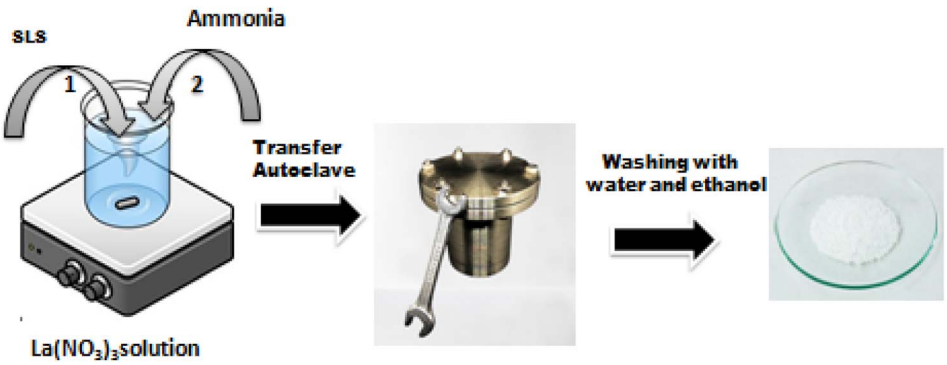

Fig. 1 Synthesis of La_2O_3 NPs.

from the samples, centrifugation was carried out at 5000 rpm for 15 minutes; the degradation of the dye was determined using a UV-visible spectrophotometer and the following formula:

$$\text{Degradation efficiency} = \frac{C_0 - C}{C_0} \times 100\%$$

where C_0 = the initial Rhodamine dye concentration, and C = the concentration of the Rhodamine dye solution after the degradation time 't'.

Results and discussion

Fourier transforms infrared spectroscopy

FT-IR spectrum of synthesized La_2O_3 NPs was obtained to identify the groups responsible for the capping and stabilization of the nanoparticles. The FTIR spectrum of the as-prepared samples was recorded in the frequency range from 4000 to 400 cm^{-1} as shown in Fig. 2.[7]

The peak at 3505 cm^{-1} was attributed to the O–H stretching of alcohols, and the peak at 3417 cm^{-1} corresponds to O–H stretching, H-bonded alcohols and phenols. The peaks located at 2922 and 2852 cm^{-1} correspond to the C–H stretching mode vibration of alkanes. The absorption peak at 1629 cm^{-1} might be due to C=C stretching (conjugated) alkenes. The peaks at around 1383 cm^{-1} and 1113 cm^{-1} represent the C–F stretching of alkyl halides and C–C stretching of ketones. The peak at 781 cm^{-1} corresponds to the C–H bending (mono) of aromatics.[23] The peak at around 619 cm^{-1} is attributed to the acetylenic C–H bending of alkynes, and that at 508 cm^{-1} is due to C–X bromoalkanes (Table 1).

Table 1 IR spectral peaks of La_2O_3 NPs

S. No	Peak (cm^{-1})	Functional group
1	3505	O–H stretch, alcohols
2	3417	O–H stretch, H-bonded alcohols, phenols
3	2922	C–H stretch, alkanes
4	2852	C–H stretch, alkanes
5	2089	C≡C terminal alkynes
6	1629	C=C stretch (conjugated), alkenes
7	1383	C–F stretch, alkyl halides
8	1113	C–C stretch, ketones
9	781	C–H bend (mono), aromatics
10	619	Acetylenic C–H bend, alkynes
11	508	C–X bromoalkanes

Structural analysis

The crystallinity and phase purity of the La_2O_3 NPs were characterized using X-ray diffraction (XRD) in the diffraction angle (2θ) range between 10° and 80°, with a scanning rate of 5° per minute.[24] The XRD pattern of La_2O_3 NPs contains several peaks as shown in Fig. 3. The obtained XRD characteristics peaks were observed at 17.61°, 25.64°, 28.08°, 29.61°, 33.98°, 42.94° and 50.2°, corresponding to the (h k l) values of the peaks (100), (004), (220), (110), (201), (210) and (116). The well-extended intensity peaks indicate the polycrystalline nature and size reduction of La_2O_3 NPs. All the identified La_2O_3 NPs peaks are in good agreement with the JCPDS card number 73-2141 and LCSD Card Number 4242, indicating the formation of the hexagonal structure of La_2O_3 NPs.[25]

The average crystallite size of the La_2O_3 NPs was found by using the Debye–Scherrer formula, where K is a constant (0.89), λ is the wavelength of X-rays (λ = 1.5418 Å), θ is the diffraction angle for the peak and β is the full width at half maximum (FWHM). The average crystallite size of the samples synthesized by this method is 41.32 nm.[26]

Particle size analyzer

The size distribution of the La_2O_3 NPs was measured *via* Dynamic Light Scattering (DLS). The DLS method examines the intensity of scattered light passing through a solution of nanoparticles. The average size is measured based on the

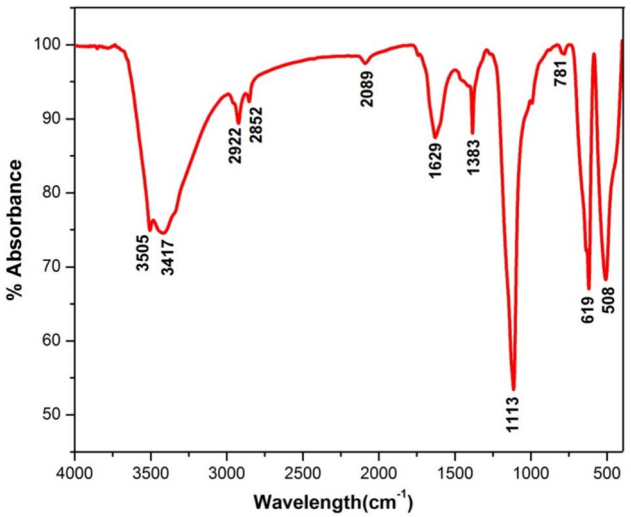

Fig. 2 FTIR spectrum of La_2O_3 NPs.

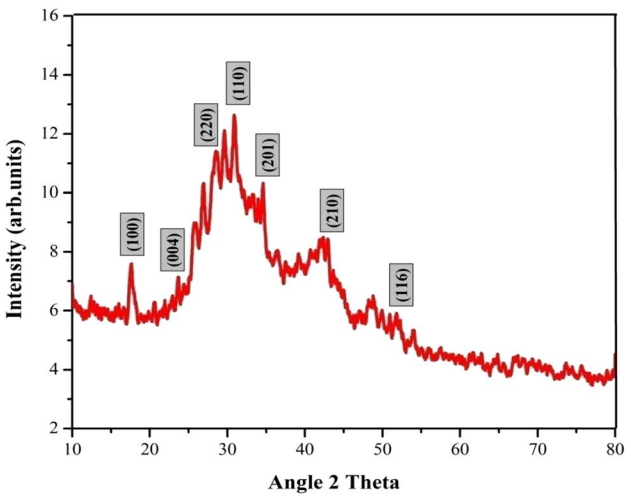

Fig. 3 XRD pattern of La_2O_3 NPs.

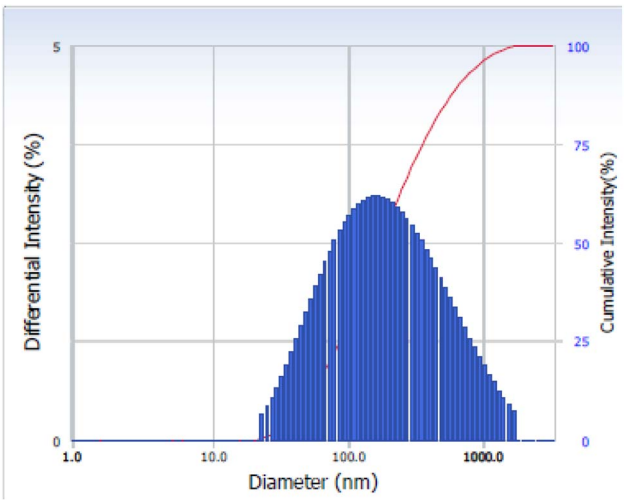

Fig. 4 PSA of La_2O_3.

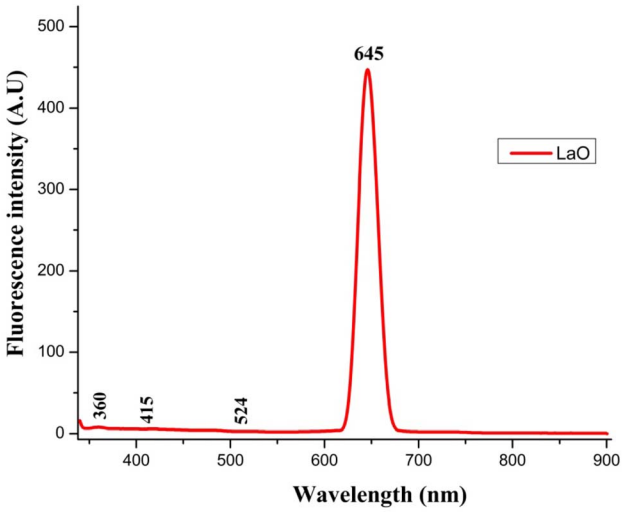

Fig. 6 Fluorescence spectrum of La_2O_3 NPs.

majority of particle sizes in a sample.[27] As observed in Fig. 4, the average size distribution of the La_2O_3 NPs is 55 nm.

Thermogravimetric analysis

The TGA of the dried La_2O_3 NPs at optimum concentration was aged for 24 h in air and was analyzed between 20 °C and 800 °C in a nitrogen atmosphere at a heating rate of 20 °C min^{-1} as shown in Fig. 5. The first weight loss for La_2O_3 was 17.10 mg in the temperature range of 50–80 °C.[28] The second weight loss was 130–129 °C; this weight loss could be attributed to the evaporation of water from the La_2O_3 accompanying the formation of $La_2O(CO_3)_2$. The third weight loss was 210–216 °C, which is attributed to the decomposition of La_2O $(CO_3)_2$. A sharp weight loss of 16.97 mg for La_2O_3 NPs occurred in the temperature range of 430–422 °C. $La_2O(CO_3)_2$ then decomposed to La_2O_3 and released CO_2, with an approximate weight loss of 28%.

Fluorescence spectroscopy

Fig. 6 depicts the fluorescence spectrum of La_2O_3 NPs as determined using a fluorescence spectrophotometer. When measuring energy levels, the fluorescence spectrum is a very significant tool.[6]

The centre of the fluorescence (FL) band appeared at 645 nm, and an increase in fluorescence intensity was observed as the size of the La_2O_3 NPs increased. These results indicate that the fluorescence emission band intensity and the absorption band of La_2O_3 NPs were dependent on the concentration and particle size.[29]

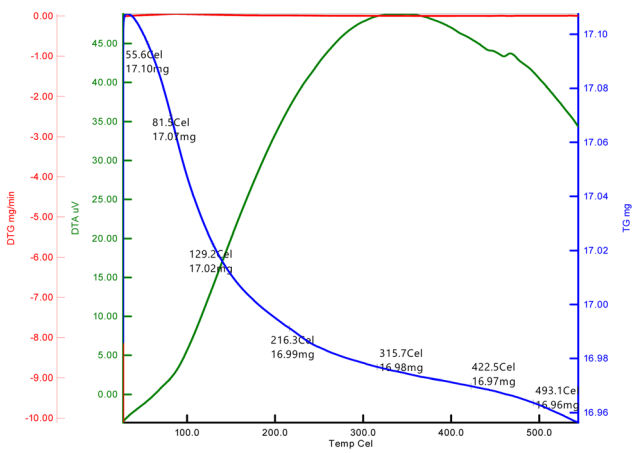

Fig. 5 TGA of La_2O_3 NPs.

Surface morphology and EDAX

The morphology and elemental composition of the products were characterized by SEM-EDS (shown in Fig. 7). The SEM images revealed that three different morphologies of La_2O_3 samples were successfully obtained, including cubic, spherical and undefined nanostructures. Fig. 7a shows that the La_2O_3 NPs tend to agglomerate; the scale bar of the image was 200 nm. The sizes of the samples were about 1, 10 and 12 mm for spherical-shaped LaO.[30]

The EDS spectrum in Fig. 7b showed the elemental composition of La and O as La_2O_3. The appearance of C elements is attributed to carbon coating the grid during the preparation process.[31]

Gas sensitivity test

For applications involving gas detection at room temperature, La_2O_3 NPs have been employed as an electrode material. Their morphological and structural characterization studies were conducted using XRD and SEM analyses.[32] When evaluating the effectiveness of a gas sensor based on a solid-state semiconductor, selectivity is an essential metric. Fig. 8 illustrates the function of produced La_2O_3 NPs on CO_2 sensing with a concentration of 50 ppm at ambient temperature.[33] The adsorption and desorption of the analyte gas over the electrode surface will cause changes in electrical parameters like conductivity and resistance. Here, the sensitivity and selectivity of the CO_2 gas during room temperature operation are significantly influenced by La_2O_3 NPs.[11]

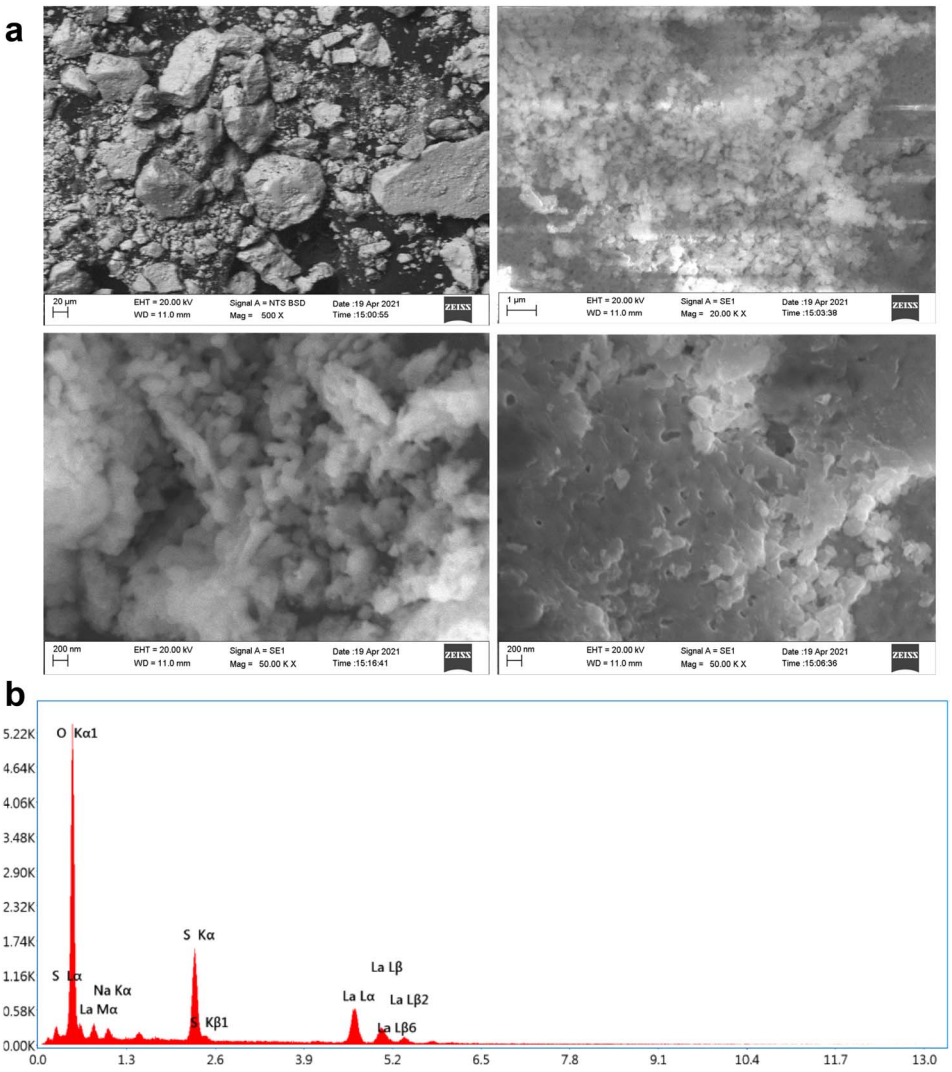

Fig. 7 (a) SEM images of La_2O_3 NPs. (b) EDAX spectrum of La_2O_3 NPs.

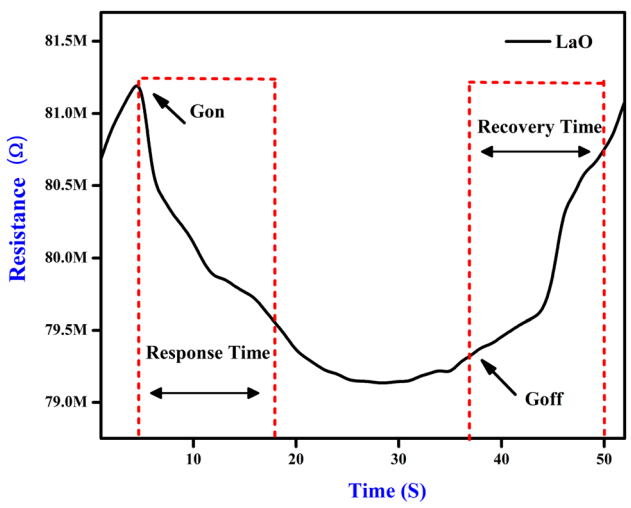

Fig. 8 Response and recovery of the La_2O_3 NPs sensing electrode.

Fig. 8 shows the response of the sensing electrodes towards 50 ppm of CO_2 at room temperature (35 °C). From the figure, we concluded that the resistance of the La_2O_3 NPs electrode decreased in the presence of CO_2 gas because the reaction area continuously adsorbed the CO_2 gas. The % sensitivity of the electrode materials was measured using eqn (1).

$$\%\ \text{sensitivity} = \frac{R_{\text{gas}} - R_{\text{air}}(\Delta R)}{R_{\text{air}}(R_{\text{a}})} \times 100 \qquad (1)$$

where R_{gas} and R_{air} are the resistance values of the sensing electrode in the presence of the target gas and air, respectively. The La_2O_3 NPs sensing electrode showed a response time of about 11 s and a 90% recovery time of about 14 s on exposure to 50 ppm ammonia gas with 80% sensitivity[34] (Table 2) (Fig. 9).

Gas selectivity test

Different gases, including H_2, O_2, NH_3, and LPG, were examined to characterise the selectivity of the sensing material, and the

Table 2 A comparison of sensing parameters with previously reported works

Sensing material	Analyte concentration	Response	Operating temperature	Reference
La/ZnO	5000 ppm	65	400 °C	35
$LaFeO_3$	2000 ppm	219	300 °C	36
CeO_2	500 ppm	22	RT	37
Ag/ZnO	100 ppm	29	150 °C	38
Al–ZnO/CuO	500 ppm	14	RT	39
La_2O_3	50 ppm	80	RT	Present work

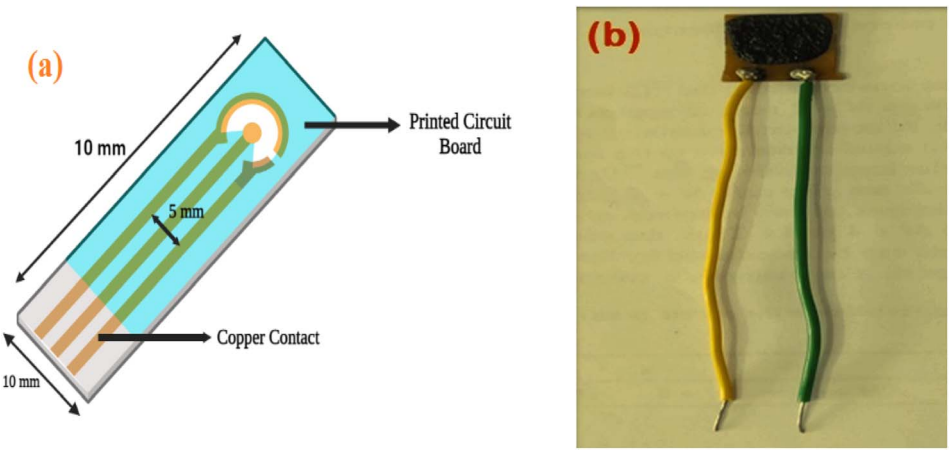

Fig. 9 (a) A schematic of the sensing electrode: (b) image of the fabricated electrode.

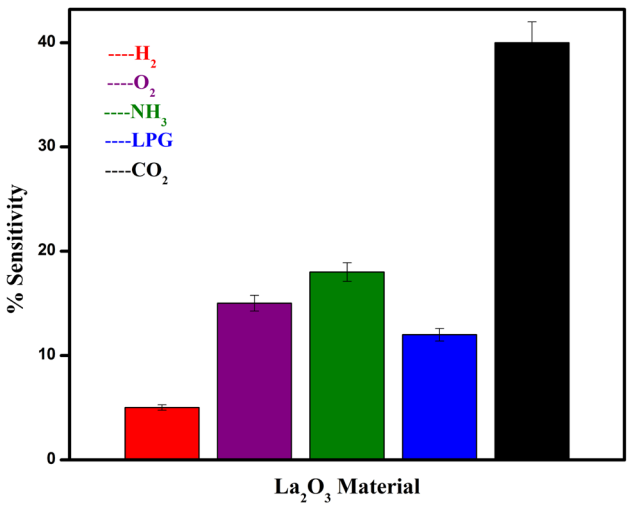

Fig. 10 The selectivity of the sensing electrodes towards various testing gases.

corresponding data is used in Fig. 10. It was observed that the La_2O_3 NPs electrodes are more sensitive to CO_2 than the other gases at ambient temperature for the same concentration.[12] Repeated selectivity tests for accuracy were conducted, and the results were displayed in a graph. The effective addition of lanthanum allowed the electrodes to selectively sense CO_2 among O_2, H_2, NH_3 and LPG.[40]

Electrode stability testing

The stability of the electrodes was examined for 50 days at 10 day intervals. The responses were noted and are shown graphically in Fig. 11. Here, 86% of the sensing readings were sustained by the electrodes La_2O_3 NPs.[2] According to the stability data, the electrodes produced better stability over a 50 day period, which was attributed to operating at room temperature. Among all the sensing electrodes tested, the La_2O_3 NPs had the greatest stability response across the testing duration.

Gas sensing mechanism

The sensing mechanism of metal oxide gas sensors must be determined for use in the design and production of new, highly effective gas sensing materials. Although the precise underlying mechanisms that trigger a gas response are still up for debate, the trapping of electrons at adsorbed molecules and the band bending caused by these charged molecules are fundamentally to blame for a change in conductivity. Based on the example of La_2O_3, a quick overview of the sensing mechanism of n-type metal oxides in air is provided below. Oxygen gas is typically adsorbed on the surface of the La_2O_3 sensing material in air.[10] The adsorbed oxygen species can absorb electrons from the La_2O_3 film's interior. The trapped negative charges of these oxygen species result in a depletion layer, which lowers the conductivity.[14]

The oxygen adsorbate-trapped electrons will return to the La_2O_3 layer when the sensor is subjected to reducing gases,

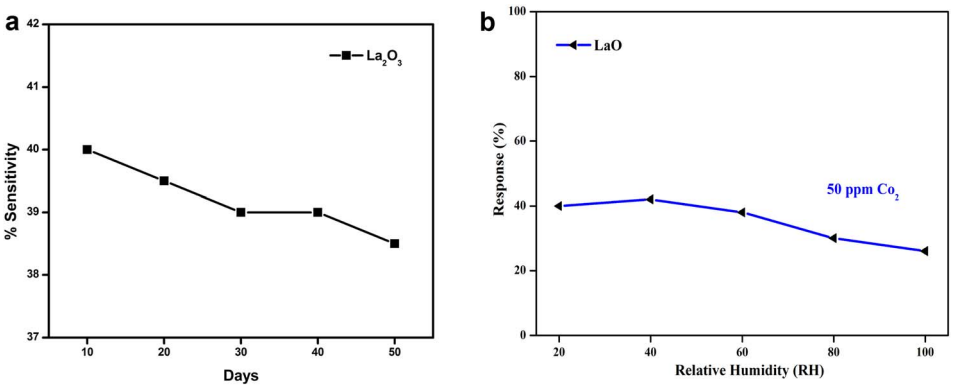

Fig. 11 (a) The stability of the sensing electrodes towards CO_2 for 50 days. (b) The sensitivity of La_2O_3 towards various relative humidity atmospheres.

resulting in a reduction in the potential barrier height and an increase in conductivity. There are different oxygen species, including molecular (O_2^-) and atomic (O^-, O^{2-}) ions, on the surface depending on the working temperature. In general, molecular forms predominate below 150 °C, while atomic species are seen beyond this temperature. For metal oxides, the surface conductivity is significantly influenced by the overall surface stoichiometry.[41] Adsorbed oxygen ions operate as surface acceptors, binding elections and decreasing surface conductivity, whereas oxygen vacancies act as donors, increasing the surface conductivity.

Fig. 12 shows the energy diagram of various oxygen species in the gas phase, adsorbed at the surface and bound within the lattice of La_2O_3. On La_2O_3 films, the reaction O_2^- ads + $e^- = 2O^-$ ads takes place as the temperature increases. The desorption temperatures from the La_2O_3 surface were around 550 °C for O^- ads ions and around 150 °C for O^{2-} ads ions.[42] At constant oxygen coverage, the transition causes an increase in the surface charge density with corresponding variations in the band bending and surface conductivity. From the conductance measurements, it was concluded that the transition takes place slowly. Therefore, a rapid temperature change on the part of the sensors is usually followed by a gradual and continuous change in the conductance.[24] The oxygen coverage adjusts to a new equilibrium and the adsorbed oxygen is converted into another species that may be used in the measurement of the dynamic modulated temperature.

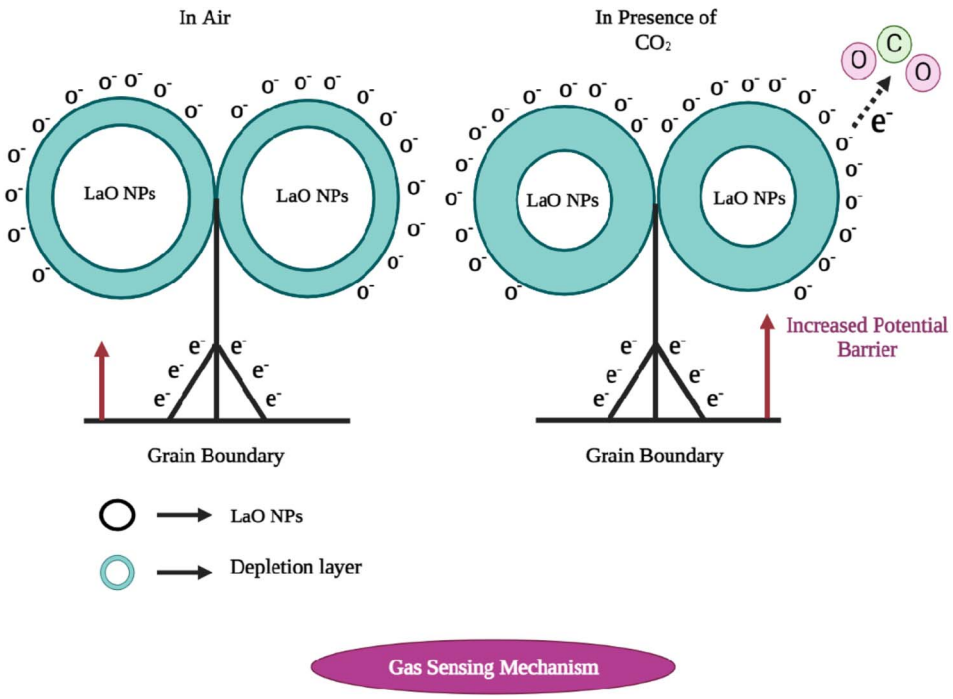

Fig. 12 The carbon dioxide sensing mechanism of La_2O_3 nanoparticles. (Left) In the presence of air, and (right) in the presence of CO_2.

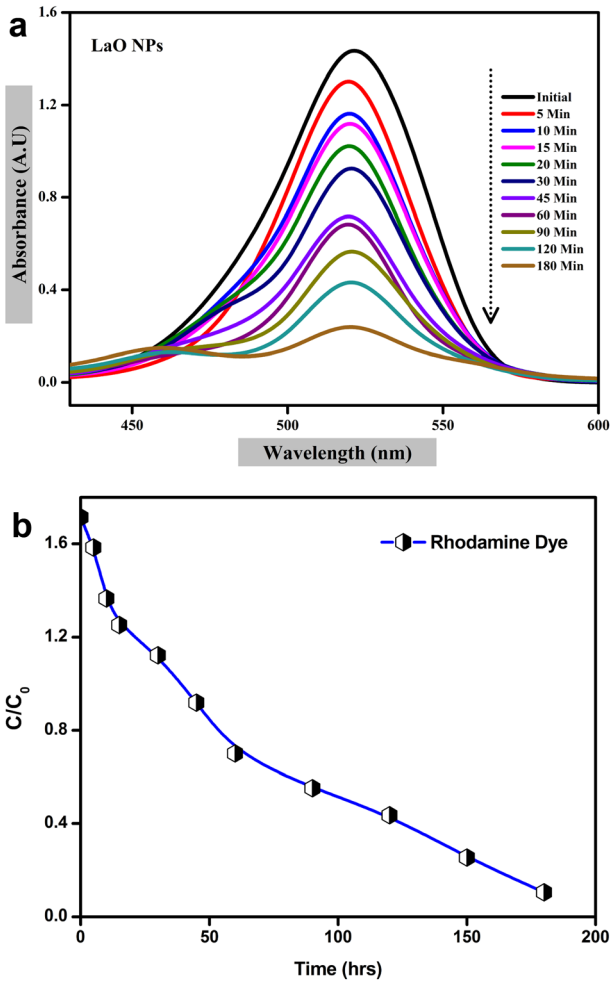

Fig. 13 Photocatalytic degradation of La_2O_3 NPs using Rhodamine dye: (a) UV visible spectra, (b) plot of C/C_0 *versus* time.

Photocatalytic activity

The photocatalytic activity of chemically synthesized La_2O_3 nanoparticles was assessed by the removal of Rhodamine dye from an aqueous solution under UV light irradiation. To determine the Rhodamine degradation, the maximum UV-vis absorption peak near 520 nm was observed and the UV light exposure time was monitored.[20] The UV-vis absorbance spectra of Rhodamine dye at different time intervals are shown in Fig. 13a.

The photolysis of Rhodamine alone was performed without any photocatalyst (blank) under UV light irradiation. As shown in Fig. 13a, about 88% of Rhodamine dye was decomposed over the La_2O_3 nanoparticles within 220 min.[43] The plot of C/C_0 *versus* the time interval showed a gradual decrease with time in the presence of synthesized La_2O_3 nanoparticles, indicating rapid degradation under UV light irradiation; the blank test showed negligible degradation of Rhodamine (Fig. 13b).

A possible photocatalytic reaction mechanism is proposed in Fig. 13. Under UV light irradiation, electrons in the valence band (VB) of La_2O_3 nanoparticles are excited into the conduction band (CB). They then migrate to the surface of the nanoparticles where the photogenerated holes react with attached OH or H_2O to produce hydroxyl radicals and the photogenerated electrons are scavenged by the O_2 dissolved in water to produce superoxide radicals.[44,45] These generated radicals participate in redox reactions with absorbed dye species and are responsible for their photocatalytic degradation. It was reported earlier that the photocatalytic activity mainly depends on the size and shape of the nanomaterials, and also the process of generation, transfer, and consumption of the photogenerated carriers.

Antibacterial activity

In the present study, the antibacterial activity of chemically synthesized La_2O_3 NPs was tested using the agar well diffusion

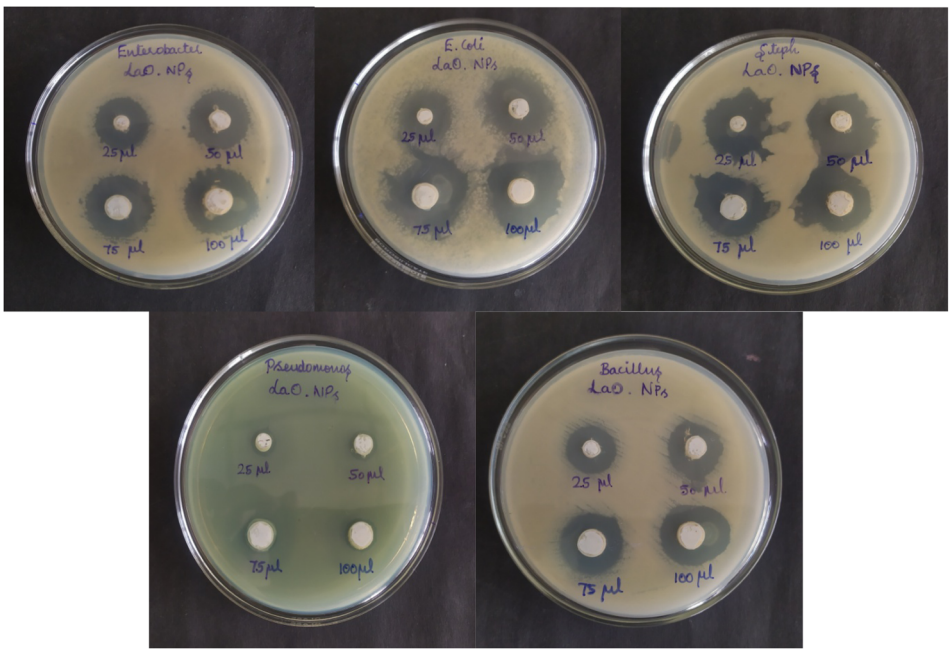

Fig. 14 Zone of inhibition of La_2O_3 NPs against various bacterial strains.

Table 3 Zone of inhibition of La_2O_3 NPs against selected bacterial strains

	Zone of inhibition (mm in diameter)				
Concentration	*Bacillus* sp.	*E. coli*	*Enterobacter* sp.	*Staphylococcus aureus*	*Pseudomonas* sp.
25 μl	1.6	1.8	1.8	2.0	0.8
50 μl	1.8	2.2	2.1	2.1	0.9
75 μl	2.1	2.5	2.2	2.4	1.1
100 μl	2.4	2.7	2.6	2.6	1.1

method against *Staphylococcus aureus*, *Bacillus subtilis*, *Enterobacter* sp., *Pseudomonas aeruginosa*, and *E. coli* (Fig. 14). La_2O_3 NPs showed an inhibition zone against the tested bacteria (Table 3). The power of La_2O_3 NPs against human pathogens was dependent on the size and dose. The synthesized La_2O_3 NPs at higher doses and smaller sizes were found to have a greater inhibitory action toward the tested bacteria.[46] The larger-sized nanoparticles showed less activity than the smaller-sized nanoparticles due to their small surface area. One of the possible modes of action of the La_2O_3 NPs might be to attach to the cell surface and disrupt the cell membrane and interact with the cell contents.[47] After penetration, the La_2O_3 NPs released lanthanum ions that interacted with DNA, proteins, and sulfur-containing cell constituents and, therefore, the organisms were inhibited.

Conclusion

We have employed a simple hydrothermal process to synthesize La_2O_3 NPs. The La_2O_3 NPs were characterized using X-Ray Diffraction (XRD), Scanning Electron Microscopy (SEM), Fourier Transform Infrared Spectroscopy (FT-IR), Fluorescence spectroscopy (FL), Particle Size Analysis (PSA), and thermogravimetric analysis (TGA). The structural, optical, and thermal properties of La_2O_3 NPs were confirmed by the characterization results. XRD studies were used to find the particulate size while scanning electron microscopy analysis of the as-synthesized powders showed spherical particles with sizes smaller than 100 nm. DLS is an analytical method used to measure the average particle size of La_2O_3 NPs. The fabricated sensor showed a high sensitivity of 40% towards CO_2 at 50 ppm. In addition, the sensor can detect concentrations up to 5 ppm with a quick response time of 6 s and recovery of 5 s. The electrode has a long-term stability of 95% for 50 days when tested with an interval of 10 days. In photocatalytic degradation, 88% of Rhodamine dye can be decomposed over the La_2O_3 nanoparticles within 220 min. Therefore, synthesizing La_2O_3 NPs could serve as an excellent application in antibacterial studies, which would help in the design of various antibodies for untreatable microbes.

Conflicts of interest

The authors declare that there are no conflicts of interest regarding the publication of this paper.

Acknowledgements

The authors would like to acknowledge the Research centre Sri Paramakalyani Centre of Excellence in Environmental Sciences, Manonmaniam Sundaranar University, Tirunelveli for giving the opportunity to carry out an important project with available resources in the laboratory.

References

1 J. Bhadra, N. J. Al-Thani, N. K. Madi and M. A. Al-Maadeed, *Synth. Met.*, 2013, **181**, 27–36.
2 H. Çolak and E. Karaköse, *Sens. Actuators, B*, 2019, **296**, 126629.
3 G. Chen, B. Han, S. Deng, Y. Wang and Y. Wang, *Electrochim. Acta*, 2014, **127**, 355–361.
4 L. Dai, G. Yang, H. Zhou, Z. He, Y. Li and L. Wang, *Sens. Actuators, B*, 2016, **224**, 356–363.
5 S. Karthikeyan, K. Dhanakodi, K. Shanmugasundaram and S. Surendhiran, *Mater. Today: Proc.*, 2021, **47**, 901–906.
6 S. Pratibha, N. Dhananjaya, A. Pasha and S. Khasim, *Appl. Nanosci.*, 2020, **10**, 1927–1939.
7 R. Sharan, M. Roy, A. K. Tyagi and A. Dutta, *Sens. Actuators, B*, 2018, **258**, 454–460.
8 H. Kabir, S. H. Nandyala, M. M. Rahman, M. A. Kabir, Z. Pikramenou, M. Laver and A. Stamboulis, *Ceram. Int.*, 2019, **45**, 424–431.
9 G. T. Adithya, S. Rangabhashiyam and C. Sivasankari, *Microchem. J.*, 2019, **148**, 364–373.
10 A. Singh, A. Singh, S. Singh, P. Tandon and B. C. Yadav, *J. Mater. Sci.: Mater. Electron.*, 2016, **27**, 8047–8054.
11 E. M. Sulaiman, U. M. Nayef and F. AH Mutlak, *Opt. Laser Technol.*, 2022, **154**, 108336.
12 T. Krishnakumar, R. Jayaprakash, T. Prakash, D. Sathyaraj, N. Donato, S. Licoccia, M. Latino, A. Stassi and G. Neri, *Nanotechnology*, 2011, **22**, 325501.
13 A. Guillén-Bonilla, O. Blanco-Alonso, J. T. Guillén-Bonilla, M. de la Luz Olvera-Amador, V. M. Rodríguez-Betancourtt, A. Sánchez-Martínez, J. P. Morán-Lázaro, M. Martínez-García and H. Guillén-Bonilla, *J. Mater. Sci.: Mater. Electron.*, 2018, **29**, 15632–15642.
14 H. Çolak and E. Karaköse, *Sens. Actuators, B*, 2019, **296**, 126629.
15 S. Naama, T. Hadjersi, A. Keffous and G. Nezzal, *Mater. Sci. Semicond. Process.*, 2015, **38**, 367–372.

16 I. Karaduman, M. Demir, D. E. Yıldız and S. Acar, *Phys. Scr.*, 2015, **90**, 055802.
17 M. Habib, S. S. Hussain, S. Riaz and S. Naseem, *Mater. Today: Proc.*, 2015, **2**, 5714–5719.
18 C. Willa, A. Schmid, D. Briand, J. Yuan and D. Koziej, *ACS Appl. Mater. Interfaces*, 2017, **9**, 25553–25558.
19 M. A. Basyooni, S. Zaki, S. Ertugrul, Y. Mucahit and Y. Eker, *Ceram. Int.*, 2019, DOI: **10.1016/j.ceramint.2019.12.259**.
20 Y. Badr, M. G. Abd El-Wahed and M. A. Mahmoud, *J. Hazard. Mater.*, 2008, **154**, 245–253.
21 A. K. Chatterjee, R. Chakraborty and T. Basu, *Nanotechnology*, 2014, **25**, 135101.
22 E. Amutha, M. Sivakavinesan, S. Rajaduraipandian and G. Annadurai, *Emergent Mater.*, 2022, DOI: **10.1007/s42247-022-00422-7**.
23 S. Srinithi, B. Arumugam, S.-M. Chen, S. Annamalai and S. K. Ramaraj, *Mater. Chem. Phys.*, 2023, **296**, 127244.
24 A. Singh and B. C. Yadav, *Surf. Interfaces*, 2022, **34**, 102368.
25 S. Sikarwar, A. Pandey, A. Singh, B. C. Yadav, I. E. Uflyand and G. I. Dzhardimalieva, *Mater. Sci. Eng., B*, 2022, **283**, 115813.
26 F. A. Ali, R. Nayak, P. G. R. Achary, D. K. Mishra, S. K. Sahoo, U. P. Singh and B. Nanda, *Mater. Today: Proc.*, 2023, **74**, 993–1001.
27 H. Zhu, C. Zhang and Y. Yin, *Nanotechnology*, 2005, **16**, 3079.
28 R. Subramaniam, A. Eswaran, G. Sivasubramanian and A. Gurusamy, *Emergent Mater.*, 2023, **6**, 261–269.
29 D. Ayodhya and G. Veerabhadram, *J. Photochem. Photobiol., B*, 2016, **157**, 57–69.
30 S. Karthikeyan, M. Selvapandiyan and A. Sankar, *Inorg. Chem. Commun.*, 2022, **139**, 109331.
31 Y.-Y. Li, L.-J. Yue, L.-H. Yue, L. Jia, J.-Q. Liu, K.-F. Xie, X.-Y. Yang and Y.-H. Zhang, *Sens. Actuators, B*, 2023, **378**, 133125.
32 S. Alamdari, M. Sasani Ghamsari and M. Jafar Tafreshi, *Nanochem. Res.*, 2017, **2**, 198.
33 R. H. Vignesh, K. V. Sankar, S. Amaresh, Y. S. Lee and R. K. Selvan, *Sens. Actuators, B*, 2015, **220**, 50–58.
34 K. Anand, J. Kaur, R. C. Singh and R. Thangaraj, *Chem. Phys. Lett.*, 2017, **682**, 140–146.
35 Y.-J. Jeong, C. Balamurugan and D.-W. Lee, *Sens. Actuators, B*, 2015, DOI: **10.1016/j.snb.2015.11.093**.
36 M. Andreev, V. Platonov, D. Filatova, E. Galitskaya, S. Polomoshnov, S. Generalov, A. Nikolaeva, V. Amelichev, O. Zhdaneev, V. Krivetskiy and M. Rumyantseva, *Sensors*, 2021, **21**, 7297.
37 P. Li, B. Wang, C. Qin, C. Han, L. Sun and Y. Wang, *Ceram. Int.*, 2020, **46**, 19232–19240.
38 M. Navaneethan, V. L. Patil, S. Ponnusamy, C. Muthamizhchelvan, S. Kawasaki, P. S. Patil and Y. Hayakawa, *Sens. Actuators, B*, 2018, **255**, 672–683.
39 M. Poloju, N. Jayababu and M. V. Ramana Reddy, *Mater. Sci. Eng., B*, 2018, 61–67.
40 S. Singh, N. Verma, A. Singh and B. C. Yadav, *Mater. Sci. Semicond. Process.*, 2014, **18**, 88–96.
41 D. V. Ponnuvelu, B. Pullithadathil, A. K. Prasad, S. Dhara, A. Ashok, K. Mohamed, A. K. Tyagi and B. Raj, *Appl. Surf. Sci.*, 2015, **355**, 726–735.
42 A. Guillén-Bonilla, O. Blanco-Alonso, J. T. Guillén-Bonilla, M. de la Luz Olvera-Amador, V. M. Rodríguez-Betancourtt, A. Sánchez-Martínez, J. P. Morán-Lázaro, M. Martínez-García and H. Guillén-Bonilla, *J. Mater. Sci.: Mater. Electron.*, 2018, **29**, 15632–15642.
43 H. Asadzadeh Patehkhor, M. Fattahi and M. Khosravi-Nikou, *Sci. Rep.*, 2021, **11**, 24177.
44 D. Fernandes, M. M. Ferrer, C. W. Raubach, M. L. Moreira, P. L. G. Jardim, E. C. Moreira, C. F. O. Graeff and S. S. Cava, *J. Am. Ceram. Soc.*, 2023, **106**, 399–409.
45 C. Nandana, M. Christeena and B. Devaraj, *J. Cluster Sci.*, 2022, **33**, 1–11.
46 S. Ameena, N. Rajesh, S. M. Anjum, H. Khadri, K. Riazunnisa, A. Mohammed and Z. A. Kari, *Appl. Biochem. Biotechnol.*, 2022, **194**, 4424–4438.
47 R. Rajamohan, C. J. Raorane, S.-C. Kim and Y. R. Lee, *Materials*, 2023, **16**, 217.